High-resolution observations of the near-infrared emission from NGC 6822 Hubble V

Sungho Lee,[1,2] Soojong Pak,[1]⋆ Sang-Gak Lee,[2] Christopher J. Davis,[3] Michael J. Kaufman,[4] Kenji Mochizuki[1] and Daniel T. Jaffe[5]

[1]*Korea Astronomy and Space Science Institute, 61-1 Whaam-dong, Yuseong-gu, Daejeon 305-348, South Korea*
[2]*Astronomy Program in SEES, Seoul National University, Shillim-dong, Kwanak-gu, Seoul 151-742, South Korea*
[3]*Joint Astronomy Centre, University Park, 660 North A'ohoku Place, Hilo, HI 96720, USA*
[4]*Department of Physics, San Jose State University, One Washington Square, San Jose, CA 95192, USA*
[5]*Department of Astronomy, University of Texas at Austin, Austin, TX 78712, USA*

ABSTRACT

We have observed Hubble V, the brightest H II region complex in the dwarf irregular galaxy NGC 6822, at near-infrared (near-IR; 1.8–2.4 μm) wavelengths. The line emission maps of Hubble V show the typical structure of a photodissociation region (PDR) where an ionized core, traced by compact He I emission (2.0587 μm) and Brγ emission (2.1661 μm), is surrounded by an outer layer traced by molecular hydrogen (H_2) emission. The measured line ratios of H_2 2–1 S(1) (2.2477 μm)/1–0 S(1) (2.1218 μm) from 0.2 to 0.6 and the unshifted and unresolved line profiles suggest that the H_2 emission originates purely from a PDR. We find no evidence for shock activity. By comparing the H_2 results with a PDR model, we conclude that Hubble V includes dense ($10^{4.5}$ cm^{-3}) and warm PDRs. In this environment, most of the H_2 molecules are excited by far-ultraviolet photons (with a field strength of 10^{2-4} times that of the average interstellar field), although collisional processes de-excite H_2 and contribute significantly to the excitation of the first vibrational level. We expect that Hubble V is in the early stage of molecular cloud dissolution.

Key words: ISM: individual: NGC 6822 (Hubble V) – ISM: lines and bands – ISM: molecules – galaxies: individual: NGC 6822 – galaxies: irregular – infrared: ISM.

1 INTRODUCTION

The dwarf irregular galaxy NGC 6822 is a member of the Local Group. Because of its proximity ($d = 500$ kpc; McAlary et al. 1983), we can resolve its molecular clouds and star-forming regions on parsec scales (1 arcsec $\simeq$ 2.4 pc). The Large Magellanic Cloud (LMC) and the Small Magellanic Cloud (SMC) are much closer to us than NGC 6822. However, they reside so close to the Galaxy that the star-forming process may be influenced by the tidal force associated with the Galactic gravitational field. On the contrary, NGC 6822 is far more isolated and star formation processes are dictated only by the local conditions in NGC 6822 itself.

The optical view of NGC 6822 is dominated by a large, well-defined, central bar and many bright H II regions and OB associations. The brightest and largest H II region complexes, Hubble I, III, V and X (Hubble 1925), are located at the northern end of the bar. The oxygen abundance measured in the H II regions [12 + log(O/H) = 8.23; Lequeux et al. 1979; Pagel, Edmunds & Smith 1980;

Skillman, Terlevich & Melnick 1989] is 2 times smaller than the Galactic value [12 + log(O/H) = 8.52 in Orion; Peimbert & Torres-Peimbert 1977] and between those in the LMC [12 + log(O/H) = 8.43] and the SMC [12 + log(O/H) = 8.02; see Dufour 1984 and the references therein]. With a total visible extent of 50 pc (about 20 arcsec on the sky), Hubble V is the brightest H II region complex in NGC 6822. Visual images show the structure of the bright core and the large, diffuse halo that surrounds the core and extends towards the northwest (O'Dell, Hodge & Kennicutt 1999; Israel et al. 2003; see Fig. 1). The core contains a compact cluster of bright blue stars. The halo is overlaid on to the eastern part of the OB association, Hodge OB 8 (O'Dell et al. 1999). The age of the Hubble V complex is about 4 Myr and there is no evidence for multiple star formation events in the past (O'Dell et al. 1999; Bianchi et al. 2001).

Wilson (1994) observed Hubble V in CO emission at high spatial resolution (6.2×11.1 arcsec) and reported finding a molecular cloud complex in the Hubble V region (Fig. 1a). According to the visual image (Fig. 1b) based on a multicolour composite from the *Hubble Space Telescope* (*HST*), it is likely that dark clouds surround all parts of the core cluster except in the west. Israel et al. (2003) found
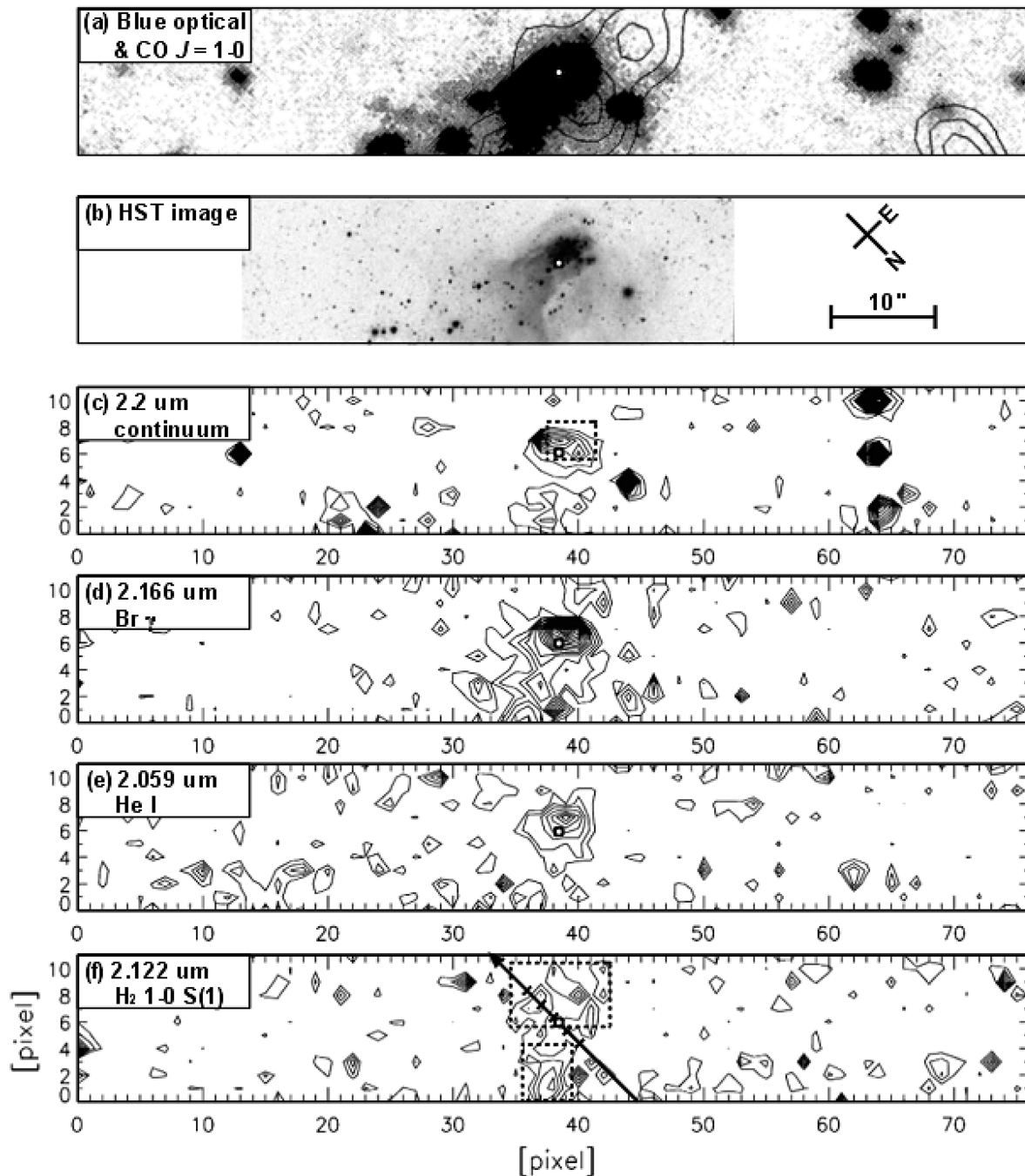
⋆E-mail: soojong@kasi.re.kr

Figure 1. (a) Blue optical image and contours of CO $J = 1$–0 integrated intensity (from Wilson 1994) over an area covered by our slit scanning observations with the 40 line mm^{-1} grating. The contour intervals are $(-4, -3, -2, 2, 3, 4, 5) \times$ Jy beam^{-1} (1σ). (b) The visual image of NGC 6822 Hubble V observed by O'Dell et al. (1999) and Bianchi et al. (2001) using the NASA/ESA/Space Telescope Science Institute (STScI) *Hubble Space Telescope* (*HST*). The four other figures of contours are reconstructed from the scanning of 12 slit positions. The horizontal axis is along the slit and each row corresponds to each slit. These contour maps show views of NGC 6822 Hubble V in (c) near-IR continuum and integrated line emission of (d) atomic hydrogen, (e) helium and (f) molecular hydrogen. Contour levels are linear and increase from 1σ rms noises with the same intervals; (c) 9×10^{-18} W m^{-2} μm^{-1} arcsec^{-2}, (d–f) 1×10^{-19} W m^{-2} arcsec^{-2}. The open circle at $(x, y) = (38.5, 6.0)$ pixel marks the position $\alpha = 19^h 44^m 52^s85$, $\delta = -14°43'12''8$ (J2000) on the sky and the pixel scale is 1.22×1.2 arcsec. The dotted boxes indicate the areas over which the spectra in Fig. 2 are averaged. The solid arrow in (f) shows the direction of the slit used for the echelle observations. The physical conditions at the five positions along the slit (marked by the ticks; hereafter positions A, B, C, D and E from the north to the south) are discussed in the text.

a compact source of K-band emission to the south of the visual core. This K-band peak is not seen in the visual images so they argued that it could be another compact star cluster that is highly obscured by the dark cloud.

In this paper, we present the results of our near-infrared (near-IR) observations of NGC 6822 Hubble V at high spatial resolutions. The observations and data reduction are described in Section 2. We present the morphology of the ionized region and photodissociation

region (PDR) and the physical conditions in the PDR in Section 3. In Section 4, we derive some physical parameters by comparing our observations with predictions of a PDR model (Sternberg & Dalgarno 1989). We also compare with previous CO observations to illustrate the structure of the molecular clouds and discuss the evolution of the Hubble V star-forming region.

2 OBSERVATIONS AND DATA REDUCTION

We observed the NGC 6822 Hubble V field at the 3.8-m United Kingdom Infrared Telescope (UKIRT) in Hawaii on 2001 June 2–4 and 2004 July 6 (UT), using the Cooled Grating Spectrometer 4 (CGS4; Mountain et al. 1990). CGS4 was set up with the 300-mm focal length camera optics and the long slit of about 90 arcsec. The observations were obtained at both low and high spectral resolution: slit scanning at low spectral resolution with the 40 line mm^{-1} grating was followed by a high-resolution spectrum with the echelle grating. The details are described in the following subsections.

Initial data reduction steps, involving bias-subtraction and flat-fielding (using an internal blackbody lamp), were accomplished by the automated Observatory Reduction and Acquisition Control (ORAC) pipeline at UKIRT. IRAF[1] was used for the remainder of the reduction. We corrected the spectral distortion along the dispersion axis using the spectrum of the standard star BS 7658 as a template. The sky OH lines for the echelle observation and Argon lines for the 40 line mm^{-1} observation were then used to correct for spatial distortion perpendicular to this axis and to wavelength calibrate the data. The telescope was nodded between on-source positions and carefully selected sky positions outside of NGC 6822; the sky frames were subtracted from the on-source frames to remove OH sky lines. Residual sky lines were removed by using blank areas on the spectral images; after subtraction of the sky lines, weak emission of H$_2$ 1–0 S(1) remained at measurable levels. At the high spectral resolving power of the echelle grating, the target H$_2$ lines were well separated from the brightest OH lines so these data do not suffer from this contamination. Details pertaining to the low- and high-resolution spectroscopic observations are given below.

2.1 *K*-band spectroscopy: slit scanning

We obtained *K*-band spectra (1.8–2.4 μm) with low spectral resolution ($\lambda/\Delta\lambda = 720$–960) using a 40 line mm^{-1} grating and a one-pixel-wide (0.61 arcsec) slit. 12 parallel slit positions were observed, sampling a 93 × 14 arcsec^2 area (Fig. 1). The slit was oriented 45° east of north for each measurement; adjacent slit positions were separated by 1.2 arcsec perpendicular to the slit length. The pixel size along the slit was 0.61 arcsec and the seeing was less than 0.44 arcsec. The image quality is degraded, however, through the optical system of CGS4 and the final spatial resolution was about 1 arcsec (2.4 pc at the distance of NGC 6822) according to the FWHM of the flux profile of the standard star along the slit.

A three-dimensional data cube was made by stacking the 12 spectral images that resulted from the slit scanning. From this cube, we extracted images of the scanned field in individual emission lines. Continuum levels were measured on either side (shortward and longward in wavelength) of each line so that the continuum emission could be accurately subtracted from each image. Figs 1(c)–

(f) show four contour maps of Hubble V, in the 2.2-μm continuum, 2.0587-μm He I, 2.1661-μm Brγ and 2.1218-μm H$_2$ 1–0 S(1) emission. Note that we have binned over two pixels along the slit axis to make the pixels roughly square in the extracted images. The final pixel scale in the reconstructed images in Fig. 1 is 1.22 × 1.2 arcsec.

At low spectral resolution, emission lines from celestial objects may not be resolved from the nearby telluric absorption lines. In this case, one cannot make a reliable flux calibration because the observed emission lines are blended with the telluric absorption profiles. However, between 2.0 and 2.3 μm, the atmospheric transmission is nearly 100 per cent and most of the emission lines of interest [2.0587-μm He I, 2.1218-μm H$_2$ 1–0 S(1), 2.1661-μm Brγ, 2.2233-μm H$_2$ 1–0 S(0) and 2.2477-μm H$_2$ 2–1 S(1)] are well separated from telluric absorption lines.

2.2 Echelle spectroscopy for H$_2$ lines

High-resolution H$_2$ 1–0 S(1) ($\lambda = 2.1218$ μm) and H$_2$ 2–1 S(1) ($\lambda = 2.2477$ μm) lines were obtained using a 31 line mm^{-1} echelle grating and a two-pixel-wide slit centred at $\alpha = 19^h44^m52\overset{s}{.}85$, $\delta = -14°43'12\overset{''}{.}8$ (J2000). The slit length was ~ 90 arcsec and the orientation was set to north–south. The position and direction of the slit is marked as an arrow in Fig. 1(f).

The slit width on the sky was 0.83 arcsec for H$_2$ 1–0 S(1) with a grating angle of 6469 and 0.89 arcsec for H$_2$ 2–1 S(1) with an angle of 6213; the pixel size along the slit was 0.90 and 0.84 arcsec, respectively, for these two configurations. Seeing was about 0.75 arcsec, but the final spatial resolution after the optics of the CGS4 was 2.1 arcsec (5.0 pc) for H$_2$ 1–0 S(1) and 1.7 arcsec (4.1 pc) for H$_2$ 2–1 S(1). The instrumental resolutions, measured from Gaussian fits to the telluric OH lines in our raw data, were ~ 17 km s^{-1} for H$_2$ 1–0 S(1) and ~ 20 km s^{-1} for H$_2$ 2–1 S(1), respectively.

The emitting region along the slit was divided into five bins (A–E) to increase the signal-to-noise (S/N) ratios. The positions of the bins are marked in Fig. 1(f) and the length of each bin is 1.8 arcsec (4.3 pc at the distance of NGC 6822). The observed spectra are presented later in Fig. 3. The emission lines are well fitted with single component Gaussian profiles and we present the fitting results in Table 1. The 1σ errors of the fitting parameters are estimated based on the rms noise of the base line of each spectrum. The average intensity [$\sim 1\,(\pm 0.1) \times 10^{-19}$ W m^{-2} arcsec^{-2}; not corrected for interstellar extinction] of our observed H$_2$ 1–0 S(1) lines is consistent with the intensity [$\sim 0.9\,(\pm 0.2) \times 10^{-19}$ W m^{-2} arcsec^{-2}] measured by Israel et al. (2003) using a large, single aperture of 19.6 arcsec in diameter. The intensities and ratios in Table 1 are corrected for the interstellar extinction. The adapted foreground reddening $E(B - V)$ to the Hubble V field is 0.65 mag ($A_V = 2.02$ mag), as suggested by Israel et al. (2003) who compare the radio continuum flux densities at 1.5, 4.8 and 10.7 GHz to the Hα flux.

3 RESULTS

3.1 Morphology in the near-IR bands

The Brγ and He I emission maps (see Fig. 1) show the morphology of the ionized region in Hubble V. Around the core, the emission of these two lines is about the same shape and size. The Brγ emission extends to the bottom of the map, towards the northwestern halo of Hubble V, where the bright stars of OB 8 should serve as the source of ultraviolet (UV) radiation. The halo part of the diffuse Brγ emission is also matched with the He I emission, although it is very weak. The morphology of our Brγ emission map is consistent

---

Table 1. Gaussian fitting parameters to the H$_2$ line profiles observed with the echelle grating.

Position[b] (arcsec)		H$_2$ 1–0 S(1) v_{LSR} (km s^{-1})	FWHM[c]	H$_2$ 2–1 S(1) V_{LSR} (km s^{-1})	FWHM[d]	$I_{1-0 S(1)}$ (10^{-19} W m^{-2} arcsec^{-2})[a]	$I_{2-1 S(1)}$	2–1 S(1)/1–0 S(1)
A	N 2.9	−36 (±2)	20 (±4)	−41 (±2)	20 (±5)	1.27 (±0.30)	0.78 (±0.28)	0.62 (±0.26)
B	N 1.1	−43 (±1)	19 (±3)	−44 (±3)	16 (±6)	1.60 (±0.31)	0.48 (±0.23)	0.30 (±0.15)
C	S 0.7	−43 (±1)	14 (±2)	−48 (±2)	14 (±5)	1.11 (±0.20)	0.60 (±0.28)	0.54 (±0.27)
D	S 2.5	−43 (±1)	14 (±1)	−44 (±3)	13 (±6)	1.70 (±0.22)	0.35 (±0.20)	0.21 (±0.12)
E	S 4.3	−41 (±2)	15 (±4)	· · ·	· · ·	0.94 (±0.35)	< 0.29	< 0.31
All[e]		−42 (±1)	17 (±1)	−44 (±1)	15 (±2)	1.28 (±0.12)	0.44 (±0.10)	0.34 (±0.09)

[a]All the integrated intensities and line ratios are corrected for an interstellar extinction of A_V = 2.02 mag. [b]Relative to α = 19^{h}44^{m}52^s.85, δ = −14°43′12″.8 (J2000) along the echelle slit. The indications are the same as in Figs 1 and 3. [c]Not corrected for instrumental broadening of ~17 km s^{-1}. [d]Not corrected for instrumental broadening of ~20 km s^{-1}. [e]The spectra of A–E are averaged.

with the 1.2822-μm Paβ emission observed by Israel et al. (2003). Our slit scanned Brγ image may be more reliable than the Paβ image of Israel et al. (2003) where the contamination by continuum was not subtracted completely using a narrow-band filter.

The H$_2$ image in Hubble V (see Fig. 1f) shows an elongated ring (with a size of 18 × 12 pc) that surrounds the brightest part of the ionized region. This kind of structure is typical of PDRs in our Galaxy (Usuda et al. 1996; Ryder et al. 1998). The more sensitive echelle observations (see Table 1) also show the distribution of H$_2$ 1–0 S(1) intensity along the slit; these data trace a cross-section through the ring-shaped H$_2$ emission mapped by the 40 line mm^{-1} observations in Fig. 1(f). Note from column 7 in Table 1 that the intensity distribution has two peaks, at positions B and D, which correspond to the two sides of the ring.

The 2.2-μm continuum image (Fig. 1c) traces the sources in the visual images (Fig. 1a and b). In the extracted continuum image, several field stars evident in the visual images are clearly seen, while the bright core and the diffuse halo of Hubble V cover the central part of the map. However, the compact source at position (x, y) = (64, 1) in Fig. 1(c) is not identified in the visual images; instead, this may be related to the nearby CO cloud at (x, y) = (71, 1), MC3 of Wilson (1994). The main body of the cloud is likely more extended than the cloud core traced by CO, because it probably obscures the compact source.

The distribution of the 2.2-μm continuum in the core region is very similar to the K-band image observed by Israel et al. (2003). Based on the infrared colours ($J − H$ = + 0.67 mag and $H − K_s$ = + 0.16 mag) derived from their wide-band photometry, they suggested that the K-band continuum peak identified by the visual cluster is dominated by radiation from K (super)giants. In K-band spectra of late-type (super)giants, the CO bandheads [e.g. 2.294-μm ^{12}CO(2,0) and 2.323-μm ^{12}CO(3,1)] should be distinct and seen in absorption (Ramírez et al. 1997). However, we do not detect the ^{12}CO(2,0) bandhead and have only a marginal detection of the (3,1) bandhead in our spectrum of the visual cluster (see Fig. 2c).

A significant fraction of the observed continuum flux can be explained by free–free or bound–free emission from the ionized region. In the spectrum averaged over the region around the core (Fig. 2a), the specific intensity at 2.2 μm is about 1 × 10^{-17} W m^{-2} μm^{-1} arcsec^{-2}, while the integrated intensity of the Brγ line is measured to be 2.94 (±0.17) × 10^{-19} W m^{-2} arcsec^{-2}. These result in the ratio of $I_{\lambda=2.2\,\mu m}/I_{Br\gamma}$ = 34 (±2) μm^{-1} (note that the scale results from the ratio of a specific intensity and a line intensity). At T_e = 11 500 K (Lequeux et al. 1979; Skillman et al. 1989), this ratio is predicted to be about 18 μm^{-1} (Osterbrock 1989). Thus,

we can conclude that more than half of the observed continuum flux is generated by the free–free or bound–free process.

The 2.2-μm continuum has two peaks in the core. One is identified with the visual star cluster while the other lies to the southwest, where there is no visual counterpart in the high-resolution *HST* image. The position of this southwestern peak is nearly identical to that of the K-band star cluster suggested by Israel et al. (2003). They argued that this new star cluster is brighter than the visual one but is obscured completely by the thick clouds of Hubble V. Our 2.2-μm continuum map shows that the southwestern peak is indeed brighter than the other peak.

It should be noted that the centres of the ionized regions, seen in the He I and Brγ emission, are not coincident with the centre of the visual star cluster. Instead, the centres are probably located midway between the two peaks in the 2.2-μm continuum map. This implies that the southern, obscured star cluster is at least as bright as the northern, visual cluster and that it is not completely embedded in the dark cloud but emits strong UV radiation in the direction of the northwestern halo part of Hubble V. In addition to this, in Section 4.1 we will show that the UV field at the position occupied by the hidden star cluster is estimated to be stronger than at other positions (see the derived parameters at position D in Table 1).

3.2 H$_2$ excitation mechanism

3.2.1 H$_2$ 2–1 S(1)/1–0 S(1) line ratio

In most cases H$_2$ line emission arises either from thermal excitation (e.g. by shock heating) or from non-thermal excitation by far-ultraviolet (hereafter far-UV) absorption (Black & van Dishoeck 1987; Burton 1992; Pak et al. 1998; Davis, Hodapp & Desroches 2001; Pak et al. 2004). One can, in principle, distinguish between these two mechanisms by comparing near-IR line intensities. The H$_2$ 2–1 S(1)/1–0 S(1) ratio has been an effective discriminant in a number of shocked regions and PDRs. Fluorescent excitation in a low-density PDR (n_{H_2} < 5 × 10^4 cm^{-3}) should yield a ratio of about 0.6. A lower ratio is expected in a denser PDR environment, where collisions populate the levels (Black & van Dishoeck 1987; Sternberg & Dalgarno 1989), or in a shock.

There are two basic types of shock; 'jump' or J-type and 'continuous' or C-type (see Draine & McKee 1993 for a review). J-type shocks (with velocities greater than about 24 km s^{-1}) will completely dissociate the molecules (Kwan 1977); H$_2$ emission occurs from a warm, recombination plateau in the post-shock region.
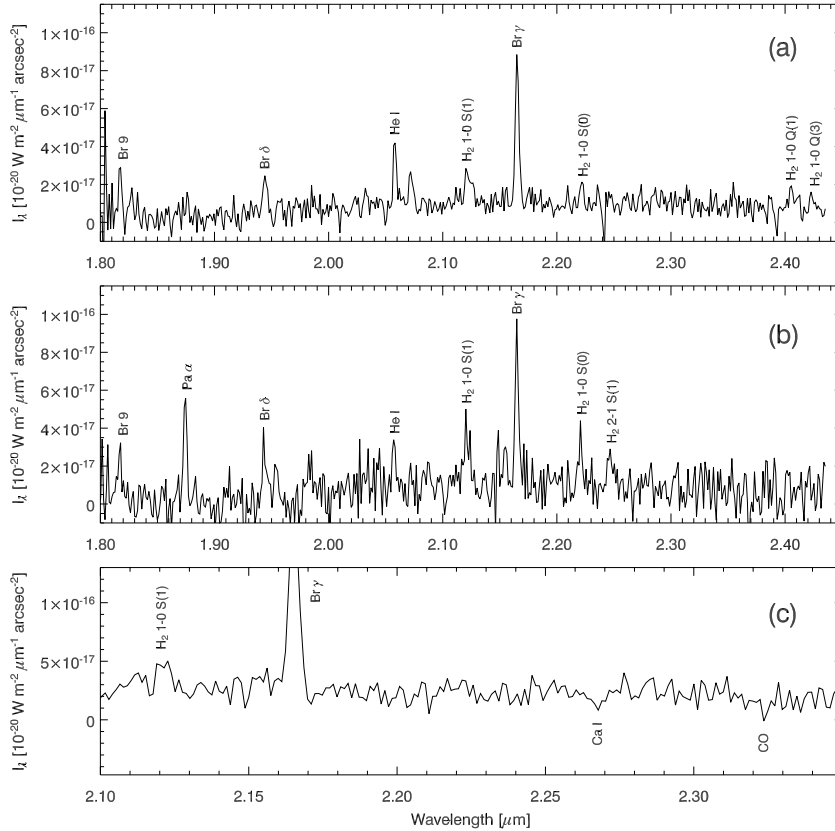
Figure 2. *K*-band spectra from the 40 line mm^{-1} grating observations. (a) 40 spectra are averaged over the 9.76×5.41 arcsec^2 area around the core (the upper dotted box in Fig. 1f). (b) 20 spectra are averaged over the 4.88×5.41 arcsec^2 area in the northwestern halo part (the lower dotted box in Fig. 1f). (c) 12 spectra are averaged over the visual cluster region of 4.88×3.01 arcsec^2 (the dotted box in Fig. 1c). No correction for the atmospheric transmission was made.

However, J-type shocks typically produce low line intensities compared with C-type shocks and H$_2$ 2–1 S(1)/1–0 S(1) line ratios as large as 0.5 possible because of formation pumping (Hollenbach & McKee 1989). At lower shock velocities, below the H$_2$ dissociation speed limit, J-type shocks may yield much lower line ratios; <0.3 (Smith 1995). In a C-type shock, where the magnetic field softens the shock front via ion-magnetosonic wave propagation the H$_2$ dissociation speed limit is much higher ($\sim$45 km s^{-1}; depending on the density and magnetic field strength in the pre-shock gas). Smaller line ratios of about 0.2 are then predicted (Smith 1995; Kaufman & Neufeld 1996). In many astronomical sources, the situation is more complicated, however, and a moderate ratio may result from a mixture of shocks and PDRs (see e.g. Fernandes, Brand & Burton 1997; Lee et al. 2003; Pak et al. 2004).

The H$_2$ 2–1 S(1)/1–0 S(1) ratios of Hubble V measured from the echelle observations are presented in Table 1. It seems that the ratios at positions A and C are consistent with PDRs. At positions B, D and E, however, we cannot distinguish between dense PDRs, J-type or C-type shocks, or a combination of these.

3.2.2 Kinematics of gas motion

Kinematic information can help distinguish between the H$_2$ excitation mechanisms. In a pure PDR environment where the H$_2$ line emission arises from the edges of neutral clouds illuminated by far-UV photons, the line profiles are narrow. J-type shocks produce narrow lines and the peak is shifted from the velocity of the pre-shock gas to that of the shock. C-type shocks, however, produce

broader lines, which peak at the velocity of the pre-shock gas and extend up to the shock velocity (e.g. Davis et al. 2000).

The H$_2$ spectra observed from Hubble V using the high-resolution echelle grating are presented in Fig. 3. Observed line profiles are very narrow (FWHM = 13–20 km s^{-1}; see Table 1). We cannot resolve the lines with the instrumental resolution of CGS4, which measured 17 and 20 km s^{-1} for H$_2$ 1–0 S(1) and H$_2$ 2–1 S(1), respectively. The measured H$_2$ line widths are consistent with those of the CO profiles (FWHMs = 4–9 km s^{-1}) observed by Wilson (1994) and Israel et al. (2003). Hence, a C-type shock interpretation may be excluded. On the other hand, we have found no noticeable shift of the H$_2$ line centres (between -36 and -48 km s^{-1} in V_{LSR}; see Table 1 and Fig. 3) from those of the CO lines (about -41 km s^{-1}; Wilson 1994; Israel et al. 2003). This result therefore excludes J-type shocks, because numerous unresolved shocks travelling in different directions would produce broad H$_2$ profiles. Hence, the kinematic data, like the excitation analysis, tend to support a non-thermal excitation mechanism.

4 DISCUSSION

4.1 Comparing with a PDR model

Given our results that the H$_2$ emission around the core region of Hubble V arises in a pure PDR environment, we can apply the observational results to a PDR model to investigate the physical conditions. The model of Sternberg & Dalgarno (1989) predicts near-IR emission spectra of molecular hydrogen in detail for a wide
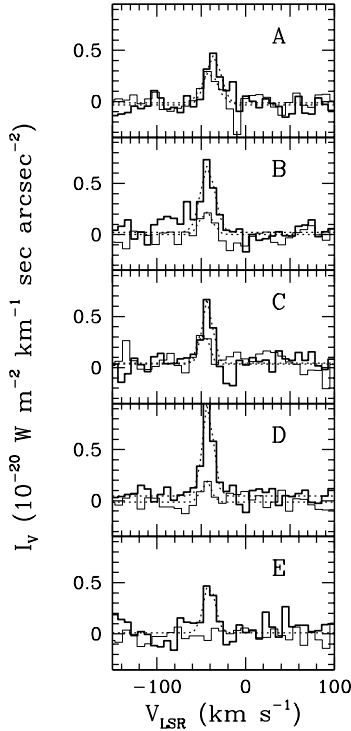
Figure 3. H$_2$ 1–0 S(1) (thick line) and H$_2$ 2–1 S(1) (thin line) spectra from the high-resolution echelle observations. The position of each spectrum labelled A–E is indicated in Fig. 1(f) and Table 1. Each spectrum is averaged over 1.8 arcsec on the sky to improve the signal-to-noise (S/N) ratios. The dotted lines are Gaussian fits to the observed line profiles. Note that the spectra are not corrected for instrumental broadening of $\sim$17 km s^{-1} for H$_2$ 1–0 S(1) and $\sim$20 km s^{-1} for H$_2$ 2–1 S(1), respectively.

range of gas density and incident UV field strength. Their model extends to dense conditions with $n_T \gtrsim 10^4$ cm^{-3}($n_T = n_H + n_{H_2}$) where collisional processes affect the distribution of the H$_2$ rovibrational levels, namely collisional fluorescence, and even farther to the thermal regime. All results quoted in this section are based on comparisons with their model.

4.1.1 Low-resolution K-band spectrum

The low-resolution spectra from the 40 line mm^{-1} observations give us hints about the physical conditions in the PDR, although quantitative analyses are difficult due to the low S/N ratios of the observed H$_2$ lines.

In the spectrum averaged over the region around the core (Fig. 2a), we can identify the H$_2$ lines of 1–0 S(1), 1–0 S(0), 1–0 Q(1) and 1–0 Q(3), but we cannot detect the 2–1 S(1) line. This H$_2$ spectrum is consistent with the models with high density ($n_T = 10^{5\,or\,6}$, almost regardless of the UV field strength, χ). The models with low density ($n_T = 10^{3\,or\,4}$) are inconsistent with the observed spectrum, because in the models the 1–0 S(0) lines are weaker than the 2–1 S(1) lines and the total intensities of the Q-branch lines are lower than those of the 1–0 S(1) lines. In our observations, the Q(1) and Q(3) lines are suppressed by telluric absorption and should be stronger than they appear in Fig. 2(a).

On the other hand, close to the northwestern halo (Fig. 2b), we can observe the 1–0 S(1), 1–0 S(0) and 2–1 S(1) lines, but we cannot detect any Q-branch lines. This spectrum resembles the model spectra of Sternberg & Dalgarno (1989) with a low density ($n_T = 10^3$).

Table 2. Gas density and the strength of the UV field derived from model comparisons.

Position[a]	A_V[b] (mag)	$n_T (= n_H + n_{H_2})$ (cm^{-3})	χ
A	2.02	$10^{4.3}$ ($10^4 < n_T \leqslant 10^{4.5}$)	10^{2-3}
B	2.02	$10^{4.5}$ ($10^{4.4} \leqslant n_T \leqslant 10^{4.7}$)	10^{2-3}
C	2.02	$10^{4.3}$ ($10^4 < n_T \leqslant 10^{4.6}$)	10^{2-3}
D	2.02	$10^{4.6}$ ($10^{4.4} \leqslant n_T \leqslant 10^{4.8}$)	10^{2-3}
	17	$10^{4.5}$ ($10^{4.5} \leqslant n_T \leqslant 10^{4.6}$)	10^{3-4}
E	2.02	$\geqslant 10^{4.4}$	10^{2-3}
	17	$\geqslant 10^{4.5}$	10^{2-3}
All	2.02	$10^{4.5}$ ($10^{4.4} \leqslant n_T \leqslant 10^{4.6}$)	10^{2-3}

[a]The positions are the same as in Table 1.
[b]Assumed interstellar extinction.

The measured line ratio of 2–1 S(1)/1–0 S(1) is 0.5 $\pm$ 0.3, which is consistent again with a low-density PDR.

4.1.2 Echelle data of H$_2$ lines

Table 2 compares the model predictions with the observed H$_2$ 1–0 S(1) line intensities and the 2–1 S(1)/1–0 S(1) ratios. In Table 1, we applied a uniform $A_V = 2.02$ mag throughout Hubble V. Israel et al. (2003), however, argued that, to the south of the core star cluster, A_V exceeds 17 mag [$E(B - V) \geqslant 5.4$ mag], because the K-band source cannot be seen in the J and H bands. Hence, we also compared the data to the models using a different extinction correction ($A_V = 17$ mag) at the two southern positions (D and E). This, however, did not change our general conclusion.

The observed intensities are consistent with the models in a range of $n_T = 10^{5\,or\,6}$ cm^{-3} and $\chi = 10^{2-4}$. Conditions of lower density ($n_T = 10^{3\,or\,4}$ cm^{-3}) cannot produce H$_2$ 1–0 S(1) intensities as strong as the observed lines, where $I_{1-0\,S(1)} \simeq 10^{-19}$ $W\,m^{-2}\,arcsec^{-2}$; the models are only marginally consistent with the observational results if we assume the strongest UV field ($\chi \gtrsim 10^4$). However, the H$_2$ 1–0 S(1) intensity is not expected to increase much more with increasing χ in the conditions of low density and high UV field [see Fig. 9 and section III(c) of Sternberg & Dalgarno 1989], because dust absorption of far-UV photons dominates over H$_2$ self-shielding (Pak et al. 2004). Moreover, the observed H$_2$ 1–0 S(1) intensities may be lower limits if the area filling factor is less than unity. Thus, it should be reasonable to exclude the case of lower density.

As for gas density, a more precise comparison is possible with the 2–1 S(1)/1–0 S(1) ratio. The ratio is insensitive to χ and can be regarded as a function of n_T when $\chi > 10^2$ (see Figs 11 and 12 of Sternberg & Dalgarno 1989). For the case of radiative fluorescent emission ($n_T \simeq 10^3$ cm^{-3}), the line ratios depend on the branching ratios of the radiative cascade. At $n_T \simeq 10^4$ cm^{-3}, where the collisional de-excitation becomes important, and at $n_T \gtrsim 10^{4.5}$ cm^{-3} with $\chi > 10^2$, where the gas becomes warm enough for collisions to dominate the excitation of the $v = 1$ levels, χ does not influence the collisional processes. Our observational results for the H$_2$ emission point to a collision-dominated model with $n_T \simeq 10^{4.5}$ cm^{-3} and $\chi = 10^{2-4}$. This means that the region around the core of Hubble V is equivalent to a dense and warm PDR, where most of the H$_2$ molecules excited by far-UV photons are collisionally de-excited and collisional processes contribute significantly to the excitation of the $v = 1$ level.

Using the measured radio continuum flux and an assumed H II region radius of 20 pc, Israel et al. (2003) found that the molecular

gas at the PDR interface is illuminated by a UV field strength $\chi = 725$. However, according to the observed distribution of the H_2 1–0 S(1) emission in this study, the front end of the interface seems to be much closer to the UV sources, at a distance of about 4 pc. If this is the case, the UV flux could be as high as $\chi = 2 \times 10^4$, which is consistent with our expectation at position D, assuming the higher extinction. By comparing the observed CO line ratios with the PDR model of Kaufman et al. (1999), Israel et al. (2003) also suggested a gas density of about 10^4 cm^{-3}. This is consistent again with our estimate to within an order of magnitude.

The Sternberg & Dalgarno (1989) model used above adopts a metallicity appropriate for our own Galaxy, whereas our observational results are for the much lower metallicity environment of NGC 6822. Kaufman et al. (1999) considered a wide range of metallicity in their PDR model, but they present no prediction for the H_2 emission. In the case of radiative fluorescence with a density of $\lesssim 10^3$ cm^{-3}, the column density, line intensity and line ratios of H_2 are known to be nearly insensitive to metallicity (Maloney & Wolfire 1996; Pak et al. 1998).

4.2 H_2 and CO in the molecular clouds

Our global view of the distribution of the H_2 emission is consistent with the CO map of Wilson (1994). Both of the H_2 features seen in Fig. 1(f), the feature surrounding the core and the feature extended into the northwestern halo, could be interpreted as being related to the MC2 cloud of Wilson (1994). As for detailed structure, however, this consistency is not maintained. The CO $J = 1$–0 brightness decreases from the north to the south by a factor of 2 or 3 (see Fig. 1 of Wilson 1994), while the H_2 1–0 S(1) intensity in the south is as bright as the emission in the north (see Table 1).

The spatial distribution of estimated gas density is shown in Table 2. The gas density seems to increase slightly from the north to the south. The lower limit at our most southern position (E) suggests that the gas density does not decrease towards the south. This is consistent with the assumption of Israel et al. (2003) of high obscuration to the south. However, the H_2 1–0 S(1) intensity rapidly decreases at the southernmost position. This contradiction may be explained if the molecular cloud is dense but has a sharp edge to the south.

The deficiency of the CO $J = 1$–0 emission to the south can be caused by a geometrical effect. The CO $J = 1$–0 emission is radiated from surfaces of CO cores because the transition is optically thick, so the intensity highly depends on the sizes of the CO cores. In a smaller molecular cloud or under a more intense UV radiation field where photodissociation makes CO cores smaller, the CO intensity should be fainter. Hence, if we assume that the southern part of the Hubble V molecular cloud has as high a density as, but a relatively smaller extent than, the northern part and it is illuminated by the obscured star cluster, which is brighter than the visual cluster, then the CO $J = 1$–0 emission should be significantly reduced at this location.

4.3 Evolution of the Hubble V complex

Leisawitz, Bash & Thaddeus (1989) surveyed 34 Galactic open clusters searching for CO clouds around each of the clusters. They found that younger clusters are associated with a larger number of more massive and bigger molecular clouds and that the clouds are receding from each of the young clusters. Leisawitz (1991) suggested that the molecular clouds should be destroyed by their interaction with newborn, hot stars and further star formation be prevented in the

cluster; massive O stars can rapidly dissolve the associated clouds by eroding the cloud surfaces with their intense radiation and by accelerating the clouds systematically with their stellar winds or via a 'rocket effect' from evaporated gases (Oort & Spitzer 1955).

We can surmise the evolutionary stage of the Hubble V complex by applying its properties to the empirical relation of Leisawitz et al. (1989) on the cloud evolution. Wilson (1994) estimated the virial masses of the Hubble V molecular clouds, MC1 and MC2, to be $< 4.6 \times 10^4$ M$_\odot$ and $< 6.3 \times 10^4$ M$_\odot$, respectively. If we adopt the estimations of Wilson (1994), the Hubble V clouds seem to be consistent with the Galactic clouds with similar ages of about 4 Myr on the evolutionary relation (see figs 43 and 47 of Leisawitz et al. 1989), both in the mass and in the proximity to the cluster; the Hubble V cluster is overlaid by the molecular clouds along the line of sight.

At first glance, the sizes of the Hubble V clouds (<18 and 52 pc for MC1 and MC2, respectively, along the major axes), reported by Wilson (1994), also look consistent with the relation of Leisawitz et al. (1989). However, the Hubble V clouds should in fact be significantly larger than the Galactic CO clouds with similar ages, because a cloud size is defined by the FWHM of the CO intensity profile in Wilson (1994), while Leisawitz et al. (1989) defined the size using the lowest contour, which is much larger than the FWHM size. Considering the low metallicity of Hubble V (with 2 times smaller [O/H] than the Galactic value), it seems consistent with the prediction of Pak et al. (1998) that the typical size of the star-forming clouds increases as the metallicity decreases.

5 CONCLUSIONS

We performed near-IR spectroscopic observations of the Hubble V complex, the brightest H II region complex in the dwarf irregular galaxy NGC 6822.

From low spectral resolution ($\lambda/\Delta\lambda \simeq 800$) K-band (1.8–2.4 μm) slit scanning, we obtained high spatial resolution (∼1 arcsec) maps of the region in the 2.2-μm continuum, 2.0587-μm He I, 2.1661-μm Brγ and 2.1218-μm H_2 1–0 S(1) emission. The morphology of Hubble V in the near-IR is typical of H II regions/PDRs; the compact He I and Brγ emitting region is surrounded by the H_2 emitting region. The detailed distribution of the H_2 emission in Hubble V is observed for the first time.

Our high spectral resolution observations ($\lambda/\Delta\lambda \simeq 15\,000$) of the H_2 1–0 S(1) and 2–1 S(1) lines, when combined with our excitation analysis, indicate that the region around the core of Hubble V is a dense PDR and suggest that there is no significant shock activity. The moderate 2–1 S(1)/1–0 S(1) ratios (0.2–0.6) are explained by high densities ($n_{H_2} \gtrsim 5 \times 10^4$ cm^{-3}) and the possibility of shocks is excluded by the gas kinematics. The H_2 lines have the same systematic velocity as the cold molecular gas (traced by CO) and the line profiles are spectrally unresolved. This conclusion implies that there is no detectable young stellar object activity around the core of Hubble V.

By comparing the observed results with a PDR model, we estimate a gas density of $n_T \simeq 10^{4.5}$ cm^{-3} and incident UV field strength of $\chi = 10^{2-4}$. This means that the environment around the core of Hubble V is dense and warm enough so that most of the H_2 molecules excited by far-UV photons are collisionally de-excited and the excitation to the $\upsilon = 1$ level is dominated by collisions. The physical parameters estimated in this work are consistent with those independently derived by Israel et al. (2003), where the strength of the UV field was estimated from radio continuum flux densities and

the gas density was estimated from CO line ratios assuming a PDR environment.

The distribution of the near-IR continuum and the line emission from the ionized regions in the southern part of Hubble V confirm the existence of a hidden star cluster inside a dark molecular cloud. Hubble V seems to be in the early stage of molecular cloud dissolution after having finished its star formation activity ~4 Myr ago. However, the progress of evolution seems slower than in the Galaxy, due to the intrinsically larger sizes and masses of the molecular clouds.

ACKNOWLEDGMENTS

REFERENCES

Bianchi L., Scuderi S., Massey P., Romaniello M., 2001, AJ, 121, 2020
Black J. H., van Dishoeck E. F., 1987, ApJ, 322, 412
Burton M. G., 1992, Aust. J. Phys., 45, 463
Davis C. J., Berndsen A., Smith M. D., Chrysostomou A., Hobson J., 2000, MNRAS, 314, 241
Davis C. J., Hodapp K. W., Desroches L., 2001, A&A, 377, 285
Draine B. T., 1978, ApJS, 36, 595
Draine B. T., McKee C. F., 1993, ARA&A, 31, 373
Dufour R. J., 1984, in van den Bergh S., de Boer K. S., eds, Proc. IAU Symp. 108, Structure and Evolution of the Magellanic Clouds. Kluwer, Dordrecht, p. 353

Fernandes A. J. L., Brand P. W. J. L., Burton M. G., 1997, MNRAS, 290, 216
Hollenbach D., McKee C. F., 1989, ApJ, 342, 306
Hubble E. P., 1925, ApJ, 62, 409
Israel F. P., Baas F., Rudy R. J., Skillman E. D., Woodward C. E., 2003, A&A, 397, 87
Kaufman M. J., Neufeld D. A., 1996, ApJ, 456, 611
Kaufman M. J., Wolfire M. G., Hollenbach D. J., Luhman M. L., 1999, ApJ, 527, 795
Kwan J., 1977, ApJ, 216, 713
Lee S., Pak S., Davis C. J., Herrnstein R. M., Geballe T. R., Ho P. T. P., Wheeler J. C., 2003, MNRAS, 341, 509
Leisawitz D., 1991, Mem. Soc. Astron. Ital., 62, 903
Leisawitz D., Bash F. N., Thaddeus P., 1989, ApJS, 70, 731
Lequeux J., Rayo J. F., Serrano A., Peimbert M., Torres-Peimbert S., 1979, A&A, 80, 155
McAlary C. W., Madore B. F., McGonegal R., McLaren R. A., Welch D. L., 1983, ApJ, 273, 539
Maloney P. R., Wolfire M. G., 1996, in Latter W. B., Radford S. J. E., Jewell P. R., Mangum J. G., Bally J., eds, Proc. IAU Symp. 170, CO: Twenty-Five Years of Millimeter-Wave Spectroscopy. Kluwer, Dordrecht, p. 299
Mountain C. M., Robertson D. J., Lee T. J., Wade R., 1990, in Crawford D. L., ed., Proc. SPIE Vol. 1235, Instrumentation in Astronomy VII. SPIE, Bellingham, p. 25
O'Dell C. R., Hodge P. W., Kennicutt R. C., Jr, 1999, PASP, 111, 1382
Oort J. H., Spitzer L., 1955, ApJ, 121, 6
Osterbrock D. E., 1989, Astrophysics of Gaseous Nebulae and Active Galactic Nuclei. University Science Books, Mill Valley, CA
Pagel B. E. J., Edmunds M. G., Smith G., 1980, MNRAS, 193, 219
Pak S., Jaffe D. T., van Dishoeck E. F., Johansson L. E. B., Booth R. S., 1998, ApJ, 498, 735
Pak S., Jaffe D. T., Stacey G. J., Bradford C. M., Klumpe E. W., Keller L. D., 2004, ApJ, 609, 692
Peimbert M., Torres-Peimbert S., 1977, MNRAS, 179, 217
Ramírez S. V., DePoy D. L., Frogel J. A., Sellgren K., Blum R. D., 1997, AJ, 113, 1411
Ryder S. D., Allen L. E., Burton M. G., Ashley M. C. B., Storey J. W. V., 1998, MNRAS, 294, 338
Skillman E. D., Terlevich R., Melnick J., 1989, MNRAS, 240, 563
Smith M. D., 1995, A&A, 296, 789
Sternberg A., Dalgarno A., 1989, ApJ, 338, 197
Usuda T., Sugai H., Kawabata H., Inoue M. Y., Kataza H., Tanaka M., 1996, ApJ, 464, 818
Wilson C. D., 1994, ApJ, 434, L11

This paper has been typeset from a TEX/LATEX file prepared by the author.